Chemical Physics Letters 629 (2015) 23–28

Contents lists available at ScienceDirect

Chemical Physics Letters

journal homepage: www.elsevier.com/locate/cplett

Photo-initiated multi-step electron transfer in donor–acceptor systems using a novel bi-functionalized perylene chromophore

Scott M. Dyar, Amanda L. Smeigh, Steven D. Karlen, Ryan M. Young, Michael R. Wasielewski*

Department of Chemistry and Argonne-Northwestern Solar Energy Research (ANSER) Center, Northwestern University, Evanston, IL 60208-3113, United States

ARTICLE INFO

Article history:
Received 5 March 2015
In final form 7 April 2015
Available online 21 April 2015

ABSTRACT

The excited state and redox properties of a new bi-functional perylene redox chromophore, 2,3-dihydro-1-azabenzo[cd]perylene (DABP), are described. Perylene has been widely used in electron donor–acceptor molecules in fields ranging from artificial photosynthesis to molecular spintronics. However, attaching multiple redox components to perylene to carry out multi-step electron transfer reactions often produces hard to separate regioisomers, which complicate data analysis. The use of DABP provides a strategy to retain the electronic properties of perylene, yet eliminate regioisomers. Ultrafast photo-initiated single- and two-step electron transfer reactions in three linear electron donor–acceptor systems incorporating DABP are described to illustrate its utility.

1. Introduction

The rational design of molecular systems capable of photo-initiated charge separation followed by charge and spin transport is important in fields ranging from artificial photosynthesis to spintronics. Perylene is an aromatic hydrocarbon that absorbs visible light at 400–450 nm to produce a 2.85 eV excited singlet state (S_1) having both electron donor and acceptor characteristics [1,2]. The perylene S_1 state can provide significant energy to drive photo-induced electron transfer reactions [3,4] that have proven useful to solar fuels [5], artificial photosynthesis [6,7], and molecule-based spintronics research [8]. The perylene S_1 state has a prominent absorption band near 700 nm [3], while its radical cation absorbs near 550 nm [8]. These distinct spectroscopic features provide a convenient way to identify these intermediates in photo-driven charge transfer reactions involving perylene.

It is often desirable to construct photo-initiated charge separation systems having multiple electron transfer steps to prolong the lifetime of the resulting radical ion pair (RP), a strategy inspired by photosynthetic reaction center proteins [9]. Incorporation of perylene into designs having strict control over donor–acceptor distances and orientations is complicated by the need to use a bi-functional perylene having a single regioisomer [10,11]; however, the synthesis of these derivatives often yields isomer mixtures that are difficult to separate [12]. In this study, we describe the properties of 2,3-dihydro-1-azabenzo[cd]perylene (DABP, Scheme 1), a new bi-functional perylene that overcomes the regioisomer problem, yet preserves the desirable electronic properties of the perylene chromophore and can readily be incorporated into multi-step electron donor–acceptor systems. We also describe photo-initiated electron transfer reactions in three electron donor–acceptor systems incorporating DABP (**1–3**, Scheme 1), which were studied using femtosecond transient absorption (fsTA), nanosecond transient absorption (nsTA), and transient electron paramagnetic resonance (TREPR) spectroscopies.

2. Experimental

2.1. Synthesis

The synthesis of **1–3** is summarized in Scheme 2 and is described explicitly in Appendix A.

2.2. Electrochemistry

Electrochemical measurements were performed on a CH Instruments model 660A electrochemical workstation. Samples were measured in a solution of 0.1 M tetra-*n*-butylammonium hexafluorophosphate ($TBAPF_6$) in acetonitrile purged with N_2 to remove

---

* Corresponding author at: Department of Chemistry, Northwestern University, 2145 Sheridan Rd., Evanston, IL 60208-3113, United States.
E-mail address: m-wasielewski@northwestern.edu (M.R. Wasielewski).

http://dx.doi.org/10.1016/j.cplett.2015.04.020
0009-2614/© 2015 Elsevier B.V. All rights reserved.

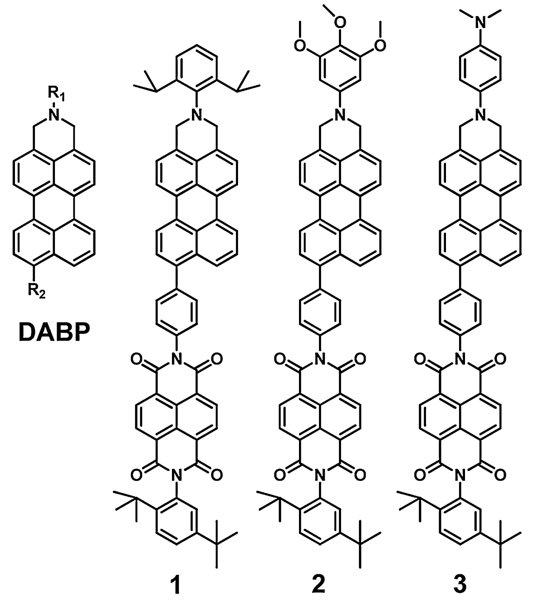

Scheme 1. Structure of DABP and donor–acceptor molecules **1–3**.

oxygen. A 1.0 mm diameter glassy carbon electrode, platinum wire counter electrode, and silver wire reference electrode were used. The ferrocene/ferrocinium couple was used as an internal reference.

2.3. Optical spectroscopy

Ground-state absorption measurements were made on a Shimadzu UV-1601 spectrophotometer. Femtosecond transient absorption (fsTA) measurements were made using the 130 fs, 416 nm frequency-doubled output from a 2 kHz regeneratively amplified Ti:sapphire laser system as the pump [13,14]. A white light continuum probe pulse was generated by focusing the IR fundamental into a 1 mm sapphire disk [15]. Samples were placed in a 2 mm path length quartz cuvette and irradiated with 1.0 μJ, 416 nm laser pulses focused to a 200 μm spot. Typically, 5–7 s of averaging was used to obtain the transient spectrum at a given delay time. The total instrument response for the pump-probe experiment was 180 fs. The optical density of all samples was maintained between 0.4 and 0.8 at 400 nm for both femtosecond and nanosecond transient absorption.

Transient absorption spectra were analyzed via singular value decomposition (SVD) using lab-written Matlab [16] programs. SVD deconvolutes the two-dimensional spectra to produce an orthonormal set of basis spectra which describe the wavelength dependence of the species and a corresponding set of orthogonal vectors which describes the time dependent amplitude of the basis spectra [17]. A species-associated first order kinetic model [18] was fit to a linear combination of the time-dependent amplitude vectors and the same linear combination of basis spectra was used to construct the spectra for the chemical species.

Nanosecond transient absorption measurements were performed using a previously described frequency-tripled Nd:YAG laser (Continuum, Precision II 8000), coupled to an optical parametric oscillator (Continuum, Panther) [5]. Low temperature experiments at 85 K were performed using a Janis VNF-100 N_2 vapor-cooled variable temperature cryostat and held at the desired temperature throughout the duration of the experiment. Samples were prepared in a nitrogen-filled glove box and placed between two quartz windows in a 2 mm path length lab-built sample holder. Kinetic traces were collected from 430 to 800 nm at 5 nm intervals, and spectra were constructed by merging the kinetic traces (binned to 12-ns steps). Each kinetic trace used to construct the

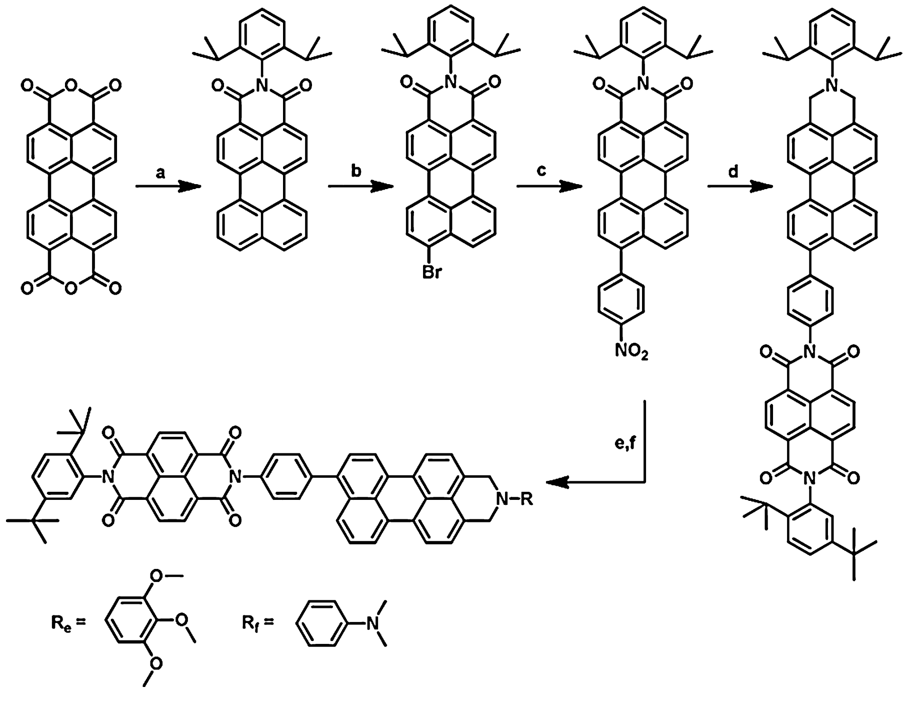

Scheme 2. (a) 2,6-Diisopropylaniline, zinc acetate dihydrate, imidazole, H_2O, 190 °C, 24 h, 61%; (b) bromine, CH_2Cl_2, reflux, 3 h, 69%; (c) *p*-(3,3,4,4-tetramethyl-2,5-dioxaborolyl)nitrobenzene, K_2CO_3, $Pd(PPh_3)_4$, toluene, ethanol, H_2O, 60 °C, 20 h, 92%; (d) (i) 1 M THF•BH_3, THF, reflux, 48 h (ii) *N*-(2,5-di-*t*-butylphenyl)-naphthalene-1,8-dicarboximide-4,5-dicarboxyanhydride, pyridine, 140 °C, 20 h, 19%; (e) (i) KOH, *t*-butanol, 100 °C, 3 h, (ii) 3,4,5-trimethoxyaniline, imidazole, 140 °C, 20 h, (iii) 1 M THF•BH_3, THF, reflux, 48 h (iv) *N*-(2,5-di-*t*-butylphenyl)-naphthalene-1,8-dicarboximide-4,5-dicarboxyanhydride, pyridine, 140 °C, 20 h, 4%; (f) (i) KOH, *t*-butanol, 100 °C, 3 h, (ii) N,N-dimethyl-*p*-phenylenediamine, imidazole, 140 °C, 20 h, (iii) 1 M THF•BH_3, THF, reflux, 48 h, (iv) *N*-(2,5-di-*t*-butylphenyl)-naphthalene-1,8-dicarboximide-4,5-dicarboxyanhydride, pyridine, 140 °C, 20 h, 2%.

spectra is representative of an average of 100 laser shots. In order to obtain decay rates, single wavelength kinetics were fit with a Levenberg–Marquardt nonlinear least squares fit to a sum of exponentials convoluted with a Gaussian instrument response function.

2.4. *EPR spectroscopy*

EPR measurements X-band (9.5 GHz) were made using a Bruker Elexsys E680-X/W EPR spectrometer outfitted with a variable *Q* dielectric resonator (ER-4118X-MD5-W1) at X-band and a cylindrical resonator (EN-680-1021H) at W-band. For EPR measurements at X-band, toluene solutions ($\sim 10^{-4}$ M) were loaded into quartz tubes (4 mm o.d. × 2 mm i.d.), subjected to four freeze-pump-thaw degassing cycles on a vacuum line (10^{-4} Torr), and sealed using a hydrogen torch. The EPR samples were stored in a dark freezer when not in use.

Transient EPR measurements were performed at X-band following photoexcitation with 7 ns, 3 mJ 416 nm pulses using the output of an optical parametric oscillator (SpectraPhysics Basiscan), pumped with the 355 nm frequency-tripled output of a Nd:YAG laser (SpectraPhysics Quanta-Ray Pro 350). Transient CW EPR spectra were collected following photoexcitation, the kinetic traces of the transient magnetization were acquired in quadrature under CW irradiation (2–20 mW). Sweeping the magnetic field gave 2D spectra with respect to both time and magnetic field. For each kinetic trace, the signal acquired prior to the laser pulse was subtracted from the data. Kinetic traces recorded at magnetic field values off-resonance were considered background signals, whose average was subtracted from all kinetic traces.

2.5. *Computational methods*

The geometry of the ground state singlet of **1–3** was initially relaxed using molecular mechanics with the MMFF294 force field, as implemented in the Avogadro 1.1.0 software [19], then subsequently relaxed using density functional theory (DFT), as implemented in the TeraChem 1.5 K software [20]. All DFT calculations made use of the unrestricted B3LYP exchange-correlation functional with a split-valence double zeta basis set with added polarization functions (6-31G*). Images of the optimized structures were generated with PyMol 1.2r1 [21]. Molecular orbitals were printed through single point energy calculations with TeraChem, using DFT (B3LYP/6-31G*), and visualized with VMD 1.9.2a27 [22].

3. Results and discussion

3.1. *Synthesis*

N-(2,6-diisopropylphenyl)-PMI was synthesized by one-pot monodecarboxylation of perylene-3,4:9,10-bis-(dicarboxyanhydride) and imide condensation of the remaining anhydride with 2,6-diisopropylaniline (Scheme 2) [23]. This species was mono-brominated using molecular bromine in dichloromethane to selectively form *N*-(2,6-diisopropylphenyl)-9-bromo-PMI. Suzuki coupling of the brominated PMI to *p*-(3,3,4,4-tetramethyl-2,5-dioxaborolyl)nitrobenzene [24] yielded *N*-(2,6-diisopropylphenyl)-9-nitrophenyl-PMI. This derivative was subjected to exhaustive reduction of its carbonyl groups with THF-BH_3 complex [25] followed by condensation with *N*-(2,5-di-*t*-butylphenyl)-naphthalene-1,8-dicarboximide-4,5-dicarboxyanhydride (NIA) [26], leaving 2,6-diisopropylaniline (An) in place on DABP to yield **1**. The remaining molecules were synthesized by first hydrolyzing *N*-(2,6-diisopropylphenyl)-9-nitrophenyl-PMI to 9-nitrophenyl-perylene-3,4-dicarboxyanhydride, then condensing it with either 3,4,5-trimethoxyaniline (TMA) or *p*-(*N*.*N*-dimethylamino)aniline (DMAA) before treatment with THF-BH_3 and condensation with NIA to form **2** or **3**, respectively.

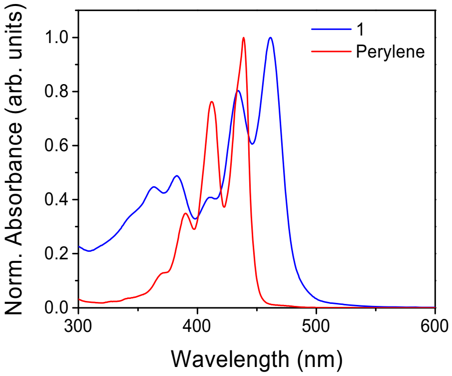

Figure 1. UV/vis absorption spectra of **1** (blue) and perylene (red) in toluene.

3.2. *Steady state measurements*

Figure 1 shows the UV–vis absorption spectrum of **1** (blue), which includes both DABP (400–500 nm) and NDI absorptions (300–400 nm) [27]. The DABP absorption is red shifted by 22 nm relative to that of unsubstituted perylene (red). Spectra of **2** and **3** are provided in Figure A1 (Appendix A). The corresponding emission spectrum of **1** in toluene is shown in Figure A2A (Appendix A). The energy of the lowest excited singlet state of DABP (^{1*}DABP), obtained from the average of the (0,0) vibronic band energies of the absorption and emission spectra, is 2.60 eV, which is somewhat lower than that of unsubstituted perylene, 2.85 eV [2].

The one-electron redox potentials of **1–3** obtained by cyclic voltammetry are given in Table 1. The NDI potentials are consistent across **1–3**; while the oxidation and reduction potentials of DABP vary over a range of 26 mV depending on the secondary donor attached to DABP through its nitrogen atom.

3.3. *Electron transfer dynamics*

Femtosecond transient absorption (fsTA) was used to probe the photo-initiated electron transfer dynamics of DABP systems **1–3** (Figure 2). Following selective excitation of DABP at 416 nm, the initial transient absorption spectrum in each case exhibits an absorption centered around 735 nm, characteristic of the perylene excited state, S_1 [2]. The $S_n \leftarrow S_1$ absorption in all three cases decays quickly due to the initial charge separation reaction (CS1).

The three-dimensional transient absorption data sets were analyzed using singular value decomposition (SVD) and global analysis (Figure A4, Appendix A) yielding, in the cases of **1** and **2**, only two species-associated components. The first component in molecules **1** and **2** shows that ^{1*}DABP decays in $\tau_{CS1} = 2.08 \pm 0.03$ and 2.20 ± 0.02 ps, respectively, concomitant with the rise of absorptions at 480 and 610 nm characteristic of NDI$^{\bullet-}$ [29], as well as a broad absorption from 500 to 650 nm assigned to DABP$^{\bullet+}$, which is consistent with spectroelectrochemistry on **2** (Figure A3, Appendix A). For **1** and **2**, the second species-associated component represents DABP$^{\bullet+}$-NDI$^{\bullet-}$ decay to ground state with lifetimes of $\tau_{CR} = 960 \pm 10$ ps and $\tau_{CR} = 1.51 \pm 0.03$ ns, respectively. No hole transfer reaction from DABP$^{\bullet+}$ to the TMA secondary donor was observed in **2**.

In the case of **3**, global analysis yields three components: the first species-associated component is assigned to ^{1*}DABP decay and the associated rise of an intermediate state, which occurs in $\tau_{CS1} = 0.53 \pm 0.02$ ps. The intermediate component, which does not correspond with DABP$^{\bullet+}$, quickly decays to NDI$^{\bullet-}$. The NDI$^{\bullet-}$ signal in this case lives significantly longer than

Table 1
One-electron redox potentials of **1–3**[a] in V vs. SCE.

	E_{Red} (NDI$^{0/-}$)	E_{Red} (NDI$^{-/2-}$)	E_{Red} (DABP$^{0/-}$)	E_{Ox} (Donor$^{0/+}$)	E_{Ox} (DABP$^{0/+}$)
1	−0.57	−1.02	−1.77	–	0.94[b]
2	−0.53	−0.96	−1.67	0.63[b]	1.08[b]
3	−0.55	−1.01	−1.53	0.11[b]	1.20[b]

[a] Recorded in acetonitrile with 0.1 M tetrabutylammonium hexafluorophosphate, a 1.0 mm diameter glassy carbon disk working electrode, a Pt wire counter electrode, and Ag wire pseudo-reference electrode. The ferrocene/ferrocenium redox couple (0.4 V vs. SCE) [28] was used as an internal standard.

[b] Irreversible couple.

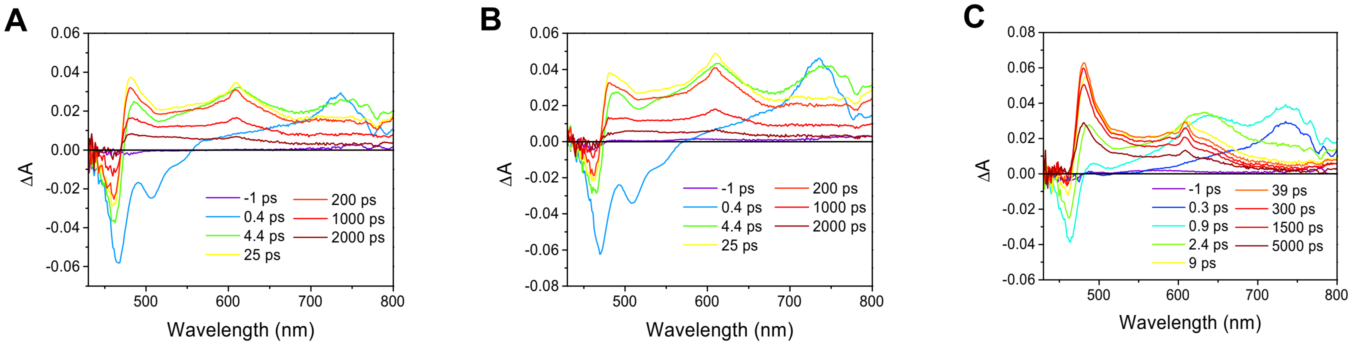

Figure 2. Femtosecond transient absorption spectra of (A) **1**, (B) **2**, and (C) **3** in toluene, exciting at λ_{ex} = 416 nm (1.0 μJ/pulse).

Table 2
Times of initial charge separation (CS1), charge shift (CS2), and charge recombination (CR) for **1–3**, obtained via SVD and global fitting.

Molecule	τ_{CS1} (ps)	τ_{CS2} (ps)	τ_{CR} (ns)
1	2.08 ± 0.03	–	0.96 ± 0.01
2	2.20 ± 0.02	–	1.51 ± 0.03
3	0.53 ± 0.02	4.76 ± 0.08	5.23 ± 0.19

Table 3
ΔG_{IP} of relevant CS states of **1–3**.

	Ion pair	ΔG_{IP} (eV)
1	An–DABP$^{+\bullet}$–NDI$^{-\bullet}$	2.53
2	TMA–DABP$^{+\bullet}$–NDI$^{-\bullet}$	2.63
2	TMA$^{\bullet+}$–DABP–NDI$^{\bullet-}$	2.46
3	DMAA–DABP$^{+\bullet}$–NDI$^{-\bullet}$	2.77
3	DMAA$^{+\bullet}$–DABP$^{-\bullet}$–NDI	2.55
3	DMAA$^{+\bullet}$–DABP–NDI$^{-\bullet}$	1.98

it does within the DABP$^{\bullet+}$–NDI$^{\bullet-}$ state observed in **1** and **2**. Based on these differences, the intermediate component is assigned to DMAA$^{\bullet+}$–DABP$^{\bullet-}$, formed via electron transfer from DMAA to ^{1*}DABP in τ_{CS1} = 0.53 ± 0.02 ps. From this intermediate state, a secondary charge shift reaction (CS2) occurs, yielding DMAA$^{+\bullet}$–DABP–NDI$^{-\bullet}$ RP, which recombines to ground state in τ_{CR} = 5.23 ± 0.19 ns. A summary of all CS and charge recombination (CR) time constants is given in Table 2.

To better understand these electron transfer dynamics, the free energy changes for the formation of relevant ion-pair states (ΔG_{IP}) in toluene were estimated using the Weller model [30] (Appendix A). These results (Table 3) provide interesting insights into the CS and CR dynamics presented above. The 2.60 eV energy of ^{1*}DABP is only slightly higher than ΔG_{IP} for An-DABP$^{\bullet+}$–NDI$^{\bullet-}$ and is nearly isoenergetic with that of TMA–DABP$^{\bullet+}$–NDI$^{\bullet-}$, both of which form after selective excitation of DABP in **1** and **2**. While the results shown in Table 3 suggest that CS2 to TMA$^{\bullet+}$–DABP–NDI$^{\bullet-}$ in **2** should be accessible, ΔG_{CS2} is only −0.14 eV, which, in this case results in a rate that is too slow to compete with CR of TMA–DABP$^{\bullet+}$–NDI$^{\bullet-}$. Analysis of the calculations relevant to **3** clearly shows why the CS order is changed relative to what is observed in **1** and **2**. ΔG_{CS1} to form DMAA–DABP$^{\bullet+}$–NDI$^{\bullet-}$ lies well above the ^{1*}DABP energy. However, DMAA is easy to oxidize, so that DMAA$^{+\bullet}$–DABP$^{-\bullet}$–NDI is accessible. After the initial CS1 step, CS2 to form DMAA$^{+\bullet}$–DABP–NDI$^{-\bullet}$ is energetically favorable.

Density functional theory (DFT) was applied to **1–3** to calculate the frontier orbitals of **1–3**, which are given in Appendix A. For **1–3**, the LUMO is consistently localized on NDI. For **1** and **2**, the HOMO is localized on DABP, which is expected for **1**, and further supports the inability of **2** to undergo CS2. For **3**, the HOMO is localized on DMAA, as expected, based on the observation of full charge separation after photoexcitation.

3.4. *Spin dynamics of **3** at 85 K*

The photo-generated singlet RP, ^{1}(DMAA$^{+\bullet}$–DABP–NDI$^{-\bullet}$) may undergo radical pair intersystem crossing (RP-ISC) driven largely by electron-nuclear hyperfine couplings in a few nanoseconds to produce the triplet RP, ^{3}(DMAA$^{+\bullet}$–DABP–NDI$^{-\bullet}$) [31,32]. The long distance between the two radicals results in a small spin–spin dipolar interaction (d) between the two radicals, which is manifest in a small zero-field splitting of the triplet RP sublevels. The dipolar interaction is averaged out in solution, but preserved when the RP is dissolved in a glassy solid. In addition, the energy gap between the nearly degenerate three triplet RP sublevels and the singlet RP is determined by the spin–spin exchange interaction ($2J$, Figure 3A). The subsequent RP recombination process is spin selective in that the singlet RP recombines to the singlet ground state, whereas the triplet RP recombines to a locally excited neutral triplet state, if this state is lower in energy than the triplet RP [33]. For DMAA–DABP–NDI, the lowest excited triplet state resides on DABP, which has a 1.5 eV energy similar to that of perylene [34]; thus, the ~2 eV energies of the triplet sublevels of ^{3}(DMAA$^{+\bullet}$–DABP–NDI$^{-\bullet}$) are about 0.5 eV above ^{3*}DABP, so that charge recombination via the triplet channel can populate DMAA–^{3*}DABP–NDI. It is worth noting that the observed DMAA$^{+\bullet}$–DABP–NDI$^{-\bullet}$ lifetime is only about a factor of 3–5 longer than that of the various initial photo-generated RPs that occur in **1–3**. This mostly likely results from the fact that ΔG for the triplet RP recombination reaction occurs in the Marcus normal region of the rate vs. free energy profile, in contrast to the

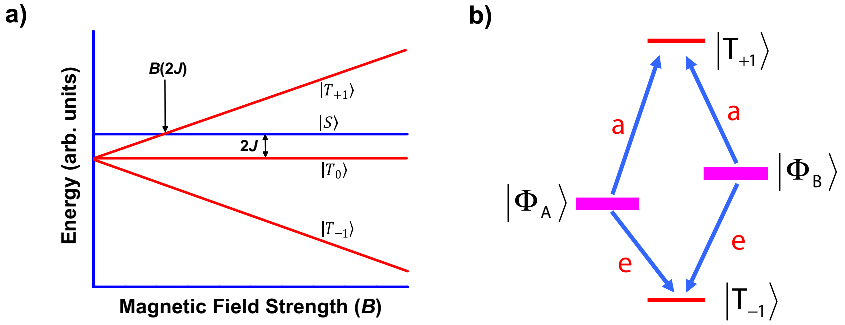

Figure 3. (a) Zeeman splitting of RP energy levels ($J > 0$); (b) relative energies of the RP spin states. Radical pair energy levels and transitions in the high magnetic field limit following S–T_0 mixing to yield Φ_A and Φ_B, which are initially populated. The arrows indicate the microwave-induced transitions responsible for the observed spin-polarized TREPR spectrum.

singlet RP recombination reaction that occurs deep into the Marcus inverted region [35,36].

TREPR spectroscopy using pulsed laser excitation and continuous microwaves was employed to directly examine DMAA$^{+\bullet}$–DABP–NDI$^{-\bullet}$. At the ~340 mT magnetic field characteristic of EPR measurements at X-band, the three RP triplet states are Zeeman split resulting in the four state energy level diagram illustrated in Figure 3B in which RP-ISC results in S-T_0 mixing to produce the coherent superposition states $|\Phi_A\rangle$ and $|\Phi_A\rangle$ [37]. Microwave-induced transitions between these states and the $|T_{+1}\rangle$ and $|T_{-1}\rangle$ states result in a spin-polarized EPR spectrum with four lines having a symmetric (*e*,*a*,*e*,*a*) anti-phase pattern (where *e* denotes emission and *a* denotes enhanced absorption, low to high field), provided that *J* is positive and larger than *d*. If the *g*-factors of the two radicals are similar and/or the transitions are split by hyperfine coupling, the two doublets will overlap significantly and appear as a distorted (*e*,*a*) signal [31,32]. The spin polarization pattern (whether a transition is *e* or *a*) is also determined by the sign rule, $\Gamma = \mu \cdot \mathrm{sign}[2J - d(3\cos^2\theta - 1)]$, where $\mu = -1$ or +1, if the spin-correlated RP is produced from a singlet or triplet precursor, respectively, and θ is the angle between the vector connecting the two spins and the externally applied magnetic field [37]. For $\Gamma = (-)$ the observed phase is (*e*,*a*) whereas for $\Gamma = (+)$ the phase is (*a*,*e*). The magnitude of *J* depends exponentially on the distance, *r*, between the individual radicals comprising the radical pair, while the dipolar interaction *d* can be determined using the point dipole approximation:

$$d = -\frac{3\mu_0 g_e^2 \beta_e^2}{8\pi r^3} \qquad (1)$$

where μ_0, g_e and β_e are the vacuum permeability, electronic *g*-factor and Bohr magneton, respectively. In units of mT and Å, $d = -2785\,\mathrm{mT\,Å}/r^3$. When a RP undergoes RP-ISC by S–T_0 mixing followed by charge recombination to yield the neutral triplet state, the six EPR transitions at the canonical (*x*,*y*,*z*) orientations relative to the applied magnetic field of the recombination triplet spectrum exhibit a unique (*a*,*e*,*e*,*a*,*a*,*e*) (low field to high field) polarization pattern [38].

Nanosecond transient absorption (nsTA) was performed on **3** in a 2-methyltetrahydrofuran (2-MTHF) glass at 85 K (see Appendix A). The DMAA$^{+\bullet}$–DABP–NDI$^{-\bullet}$ RP forms within the 7 ns instrument response of the experiment and decays in $\tau_{CR} = 16.7\,\mu$s. Photoexcitation of **3** at 85 K yields a long-lived spin-correlated RP with a TREPR spectrum visible immediately following the instrument response (~70 ns) having an (*e*,*a*) pattern [39], which is superimposed on the spin-polarized spectrum of DMAA-^{3*}DABP-NDI (Figure 4A). The RP spectrum decays as the neutral triplet spectrum appears and is followed by final decay of the neutral triplet spectrum. Figure 4A gives the full spectrum collected at 160 ns following the laser pulse, while Figure 4B gives an expanded, baseline-corrected spectrum focusing on the narrower RP signal from the same spectrum. Simulation of the RP spectrum yields $|J| = 0.7$ mT and $d = -0.2$ mT. Using Eq. (1), the dipolar interaction yields a 24 Å distance between DMAA$^{+\bullet}$ and NDI$^{-\bullet}$ in **3**, which is very close to the 23 Å RP distance predicted using DFT (B3LYP/6-31G*) calculations (Table A2, Appendix A). Simulation of the TREPR spectrum of DMAA-^{3*}DABP-NDI yields zero-field splittings $D = 56.4$ mT and $|E| = 2.7$ mT with sublevel populations $T_x = 0.45$, $T_y = 0.61$, and $T_z = 0.45$. This simulation shows that DMAA–^{3*}DABP–NDI is formed by contributions from

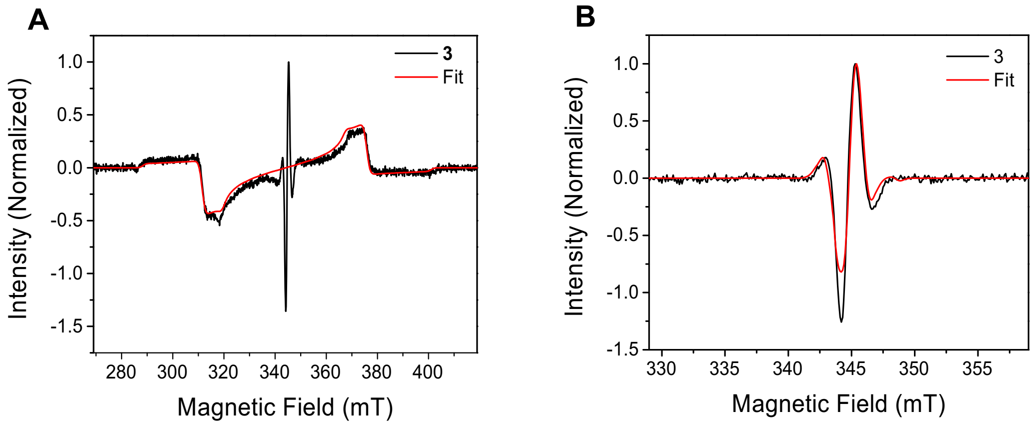

Figure 4. (A) Full and (B) expanded spectra of **3** in 2-MTHF (85 K) 160 ns after excitation at $\lambda_{ex} = 450$ nm (1.8 mJ/pulse). The red, superimposed curves are simulations performed with parameters given in the text.

both the RP-ISC and SO-ISC mechanisms. RP recombination of $DMAA^{+\bullet}$–DABP–$NDI^{-\bullet}$ via RP-ISC to DMAA–^{3*}DABP–NDI (58%) is accompanied by fast triplet formation via charge recombination of the initial singlet RP state $DMAA^{\bullet+}$–$DABP^{\bullet-}$–NDI directly to DMAA–^{3*}DABP–NDI (42%) by the so-called spin–orbit charge transfer (SOCT) mechanism, which has been observed previously [39]. The data imply that at 85 K the quantum yield of complete charge separation in **3** to yield $DMAA^{+\bullet}$–DABP–$NDI^{-\bullet}$ is 58%.

4. Conclusions

The DABP chromophore can be synthesized from well-known starting materials and is easily incorporated into systems comprising common donors, acceptors, and chromophores. DABP performs similarly to, but offers advantages over perylene, particularly by avoiding regioisomers in the preparation of bi-functionalized perylene-based donor–acceptor triads, by providing accessible connectivity to a secondary donor, and by facilitating charge-shift reactions to a secondary donor that incorporates the electron-rich amine of DABP as part of its structure. Thus DABP is a new building block with significant advantages for the rational design of electron-transfer systems having controlled distances and orientations between their redox partners.

Acknowledgement

This work was supported by the National Science Foundation under grant no. CHE-1266201.

Appendix A. Supplementary data

Supplementary data associated with this article can be found, in the online version, at doi:10.1016/j.cplett.2015.04.020

References

[1] C.R. Goldschmidt, M. Ottolenghi, J. Phys. Chem. 75 (1971) 3894.
[2] N. Sabbatini, M.T. Indelli, M.T. Gandolfi, V. Balzani, J. Phys. Chem. 86 (1982) 3585.
[3] W.B. Davis, M.A. Ratner, M.R. Wasielewski, Chem. Phys. 281 (2002) 333.
[4] K.E. Brown, B.S. Veldkamp, D.T. Co, M.R. Wasielewski, J. Phys. Chem. Lett. 3 (2012) 2362.
[5] B.S. Veldkamp, W.S. Han, S.M. Dyar, S.W. Eaton, M.A. Ratner, M.R. Wasielewski, Energy Environ Sci 6 (2013) 1917.
[6] S.M. Dyar, J.C. Barnes, M. Juricek, J.F. Stoddart, D.T. Co, R.M. Young, M.R. Wasielewski, Angew. Chem. Int. Ed. Engl. 53 (2014) 5371.
[7] R.M. Young, S.M. Dyar, J.C. Barnes, M. Juricek, J.F. Stoddart, D.T. Co, M.R. Wasielewski, J. Phys. Chem. A 117 (2013) 12438.
[8] L. Kobr, D.M. Gardner, A.L. Smeigh, S.M. Dyar, S.D. Karlen, R. Carmieli, M.R. Wasielewski, J. Am. Chem. Soc. 134 (2012) 12430.
[9] R.E. Blankenship, Molecular Mechanisms of Photosynthesis, Blackwell Science, Oxford, 2002.
[10] H.-F. Chen, D.M. Gardner, R. Carmieli, M.R. Wasielewski, Chem. Commun. 49 (2013) 8614.
[11] T. Miura, R. Carmieli, M.R. Wasielewski, J. Phys. Chem. A 114 (2010) 5769.
[12] A. Zinke, F. Linner, O. Wolfbauer, Chem. Ber. 58 (1925) 323.
[13] E.A. Weiss, M.J. Ahrens, L.E. Sinks, A.V. Gusev, M.A. Ratner, M.R. Wasielewski, J. Am. Chem. Soc. 126 (2004) 5577.
[14] S.R. Greenfield, M.R. Wasielewski, Opt. Lett. 20 (1995) 1394.
[15] J.M. Giaimo, A.V. Gusev, M.R. Wasielewski, J. Am. Chem. Soc. 124 (2002) 8530.
[16] MATLAB, The MathWorks, Inc., Natick, MA, 2013.
[17] E.R. Henry, J. Hofrichter, Methods Enzymol. 210 (1992) 129.
[18] T.M. Zamis, L.J. Parkhurst, G.A. Gallup, Comput. Chem. (Oxford) 13 (1989) 165.
[19] M.D. Hanwell, K. Lutz, Abstracts of Papers of the American Chemical Society, vol. 244, 2012.
[20] I.S. Ufimtsev, T.J. Martinez, J. Chem. Theory Comput. 5 (2009) 2619.
[21] L.L.C. Schrodinger, The PyMOL Molecular Graphics System, Version 1.3r1, 2010.
[22] W. Humphrey, A. Dalke, K. Schulten, J. Mol. Graphics Modell. 14 (1996) 33.
[23] K.M. Lefler, K.E. Brown, W.A. Salamant, S.M. Dyar, K.E. Knowles, M.R. Wasielewski, J. Phys. Chem. A 117 (2013) 10333.
[24] M.J. Ahrens, L.E. Sinks, B. Rybtchinski, W.H. Liu, B.A. Jones, J.M. Giaimo, A.V. Gusev, A.J. Goshe, D.M. Tiede, M.R. Wasielewski, J. Am. Chem. Soc. 126 (2004) 8284.
[25] S.Y. Hsu, L.Y. Chiang, Synth. Commun. 19 (1989) 1885.
[26] R. Carmieli, Q.X. Mi, A.B. Ricks, E.M. Giacobbe, S.M. Mickley, M.R. Wasielewski, J. Am. Chem. Soc. 131 (2009) 8372.
[27] M.T. Colvin, R. Carmieli, T. Miura, S. Richert, D.M. Gardner, A.L. Smeigh, S.M. Dyar, S.M. Conron, M.A. Ratner, M.R. Wasielewski, J. Phys. Chem. A 117 (2013) 5314.
[28] N.G. Connelly, W.E. Geiger, Chem. Rev. 96 (1996) 877.
[29] D. Gosztola, M.P. Niemczyk, W. Svec, A.S. Lukas, M.R. Wasielewski, J. Phys. Chem. A 104 (2000) 6545.
[30] A. Weller, Z. Phys. Chem. 133 (1982) 93.
[31] G.L. Closs, M.D.E. Forbes, J.R. Norris, J. Phys. Chem. 91 (1987) 3592.
[32] P.J. Hore, D.A. Hunter, C.D. Mckie, A.J. Hoff, Chem. Phys. Lett. 137 (1987) 495.
[33] E.A. Weiss, M.A. Ratner, M.R. Wasielewski, J. Phys. Chem. A 107 (2003) 3639.
[34] S.L. Murov, I. Carmichael, G.L. Hug, Handbook of Photochemistry, Marcel Dekker, New York, 1993.
[35] R.A. Marcus, J. Chem. Phys. 24 (1956) 966.
[36] R.A. Marcus, J. Chem. Phys. 43 (1965) 679.
[37] P.J. Hore, in: A.J. Hoff (Ed.), Advanced EPR in Biology and Biochemistry, Elsevier, Amsterdam, 1989, p. 405.
[38] H. Levanon, J.R. Norris, Chem. Rev. 78 (1978) 185.
[39] Z.E.X. Dance, S.M. Mickley, T.M. Wilson, A.B. Ricks, A.M. Scott, M.A. Ratner, M.R. Wasielewski, J. Phys. Chem. A 112 (2008) 4194.